Indonesian Journal of Maritime Technology (ISMATECH)
Vol. 04, Issue 01, June 2026
eISSN: 3025-518X
DOI: https://doi.org/10.35718/ismatech.v4i1.8481984

Comparative Analysis of Turbulence Models for Gawn Series Propeller using CFD Method

Adhyve Priambodo Bhaskara[1], I Ketut Suastika[1*], Mahendra Indiaryanto[2], Taufiq Arif Setyanto[2], Amalia Ika Wulandari[3], Dimas Fajar Prasetyo[4]

[1]Department of Naval Architecture, Sepuluh Nopember Institute of Technology, Surabaya, 60111, Indonesia
[2]Research Center of Hydrodynamics Technology, National Research and Innovation Agency, Surabaya, 60117, Indonesia
[3]Department of Naval Architecture, Kalimantan Institute of Technology, Balikpapan, 76127, Indonesia
[4]School of Earth and Oceans, The University of Western Australia, Perth, 6009, Australia

KEYWORDS
Gawn Series Propeller;
CFD;
RANS;
Thrust Coefficient;
Torque Coefficient

ABSTRACT – The rapid advancement of computational technology has positioned Computational Fluid Dynamics (CFD) as an effective tool for predicting marine propeller hydrodynamic performance. This study applies a CFD-based numerical method using Reynolds-Averaged Navier–Stokes (RANS) equations to evaluate and compare the accuracy of three turbulence models, namely k–ε, k–ω, and k–ω SST for a Gawn Series marine propeller. CFD simulations were conducted by varying the advance coefficient (J). Verification of the results for each turbulence model was carried out through Grid Independence Study and Grid Convergence Index analysis. The CFD simulation results were then compared with experimental test data using the Root Mean Square Error (RMSE) method, with K_T, $10K_Q$, and efficiency as evaluation parameters. The results demonstrate that the k–ω SST model provides the most consistent and accurate predictions across the entire operating range, with RMSE values of 1.24% for K_T, 1.98% for $10K_Q$, and 1.88% for efficiency. Pressure-contour visualization from the k–ω SST model shows the smoothest pressure distribution on the blade surface, while pathline visualization reveals the clearest, most consistent, and well-balanced vortex structures downstream of the propeller, thereby providing a robust and reliable basis for selecting the most suitable turbulence model to improve the accuracy of CFD-based marine propeller performance prediction.

*Corresponding Author | I Ketut Suastika | ✉ (suastika@its.ac.id)

INTRODUCTION

In the maritime sector, propellers play a crucial role in maximizing the thrust generated by ship engines, thereby directly influencing vessel efficiency, operational performance, and fuel consumption [1][2][3]. Marine propellers are available in various types, each designed to meet specific operational requirements. Among these, the Gawn Series propeller has attracted considerable attention due to its favorable hydrodynamic characteristics. Gawn Series propellers are capable of generating optimal induced velocity in both tangential and axial directions, which enhances thrust production and improves energy efficiency [4][5]. The propeller is designed with an optimized pitch-to-diameter (P/D) ratio and expanded blade area, resulting in high thrust and torque output. Owing to these design features, Gawn Series propellers are particularly suitable for high-speed vessels, as they exhibit reliable and consistent performance across a wide range of operating speeds, from low to high advance conditions [6][7].

With the rapid advancement of computational technology, Computational Fluid Dynamics (CFD) has emerged as a powerful numerical tool for simulating fluid-flow phenomena. CFD provides high-accuracy predictions of flow behavior without the need for extensive experimental testing, which is often costly, time-consuming, and experimentally complex. Within CFD analyses, Reynolds-Averaged Navier–Stokes (RANS) turbulence models are widely employed to predict turbulent flow characteristics, including pressure and velocity distributions around marine propellers. By decomposing the instantaneous flow into mean and fluctuating components, RANS-based approaches yield governing equations that are computationally feasible while retaining essential turbulent-flow physics [8].

However, previous studies have indicated that conventional turbulence models, such as the k–ε model, may lead to considerable prediction errors under specific flow conditions, particularly in cases involving flow transition or strong adverse pressure gradients [9]. Moreover, the complex geometry of marine propellers combined with rotational effects renders CFD simulations highly sensitive to numerical configurations, including mesh

resolution, computational domain size, and the selection of turbulence models [10]. These issues highlight the absence of a clear consensus on the most suitable RANS turbulence model for achieving accurate and reliable marine propeller performance prediction.

Based on these considerations, the present addresses an urgent need for a systematic and validated comparison of widely used RANS turbulence models applied to marine propeller analysis. The present research investigates the hydrodynamic performance of a Gawn Series G4-828 propeller using CFD simulations with various RANS turbulence models. The accuracy and effectiveness of each turbulence model in predicting thrust and torque are evaluated by comparing numerical results with laboratory experimental data. Through this comparative assessment, the research seeks to identify the most suitable RANS turbulence model for the CFD-based analysis of marine propeller performance.

METHODS

This research employs a CFD–based numerical approach to investigate the hydrodynamic performance of a Gawn Series G4-828 propeller. The overall methodology is systematically structured into five main stages:

1. Formulation of the governing equations and data collection.
2. Geometry and computational domain modelling.
3. Mesh generation.
4. CFD solver setup.
5. Verification and validation of the simulation results.

Governing Equations

The governing equations employed in this research are used to evaluate the dimensionless performance parameters, namely the thrust coefficient (K_T), torque coefficient (K_Q), advance coefficient (J), and propeller efficiency (η_0). In addition, the Reynolds-Averaged Navier–Stokes (RANS) equations are applied to model turbulent flow behavior in the numerical simulations.

The thrust coefficient is derived from the thrust force generated by the propeller as a result of accelerating the water mass in the downstream direction, which produces an equal and opposite reaction force that propels the vessel forward. The thrust force is expressed as [11]:

$$T = \rho n^2 D^4 K_T \tag{1}$$

The torque coefficient is obtained from the torque required by the engine to rotate the propeller against hydrodynamic drag. Torque arises due to blade drag and the resistance of the surrounding fluid to propeller rotation. The torque equation is given as [11]:

$$Q = \rho n^2 D^5 K_Q \tag{2}$$

Propeller efficiency represents the ratio between the effective power used to propel the vessel forward and the power delivered to the propeller through the engine torque. The open-water efficiency is calculated as follows [11]:

$$\eta_o = \frac{K_T}{K_Q}\frac{J}{2\pi} \tag{3}$$

where the advance coefficient is defined as:

$$J = \frac{V_A}{nD} \tag{4}$$

The RANS equations represent a set of nonlinear partial differential equations that are inherently complex in turbulent-flow analysis. Although the instantaneous Navier–Stokes equations are theoretically capable of describing all turbulent flow scales, their strong nonlinearity makes direct analytical solutions impractical [12]. Consequently, a numerical approach is adopted by decomposing flow variables into mean and fluctuating components, leading to the RANS formulation for turbulent-flow modeling. The continuity and momentum equations are expressed as follows:

$$\nabla = [\rho U] \tag{5}$$

$$\frac{\partial[\rho U]}{\partial t} + \nabla\{\rho UU\} = -\nabla P + [\nabla\{\bar{\tau} - \rho\overline{u'u'}\}] + \rho g \tag{6}$$

Based on the continuity and momentum equations, turbulence closure is achieved using various RANS turbulence models, including the k–ε, k–ω, and k–ω SST models. The k–ε turbulence model is formulated using two transport equations: the turbulent kinetic energy kkk and its dissipation rate ε\varepsilonε. These equations are given as [12]:

$$\frac{\partial k}{\partial t} + \mu_j \frac{\partial k}{\partial x_j} = P - \epsilon + \frac{\partial}{\partial x_j}\left[\left(\nu + \frac{\nu t}{\sigma k}\right)\frac{\partial k}{\partial x_j}\right] \quad (7)$$

$$\frac{\partial \epsilon}{\partial t} + \mu_j \frac{\partial \epsilon}{\partial x_j} = C_{\epsilon 1}\frac{\epsilon}{k}P - C_{\epsilon 2}\frac{\epsilon^2}{k}P + \frac{\partial}{\partial x_j}\left[\left(\nu + \frac{\nu t}{\sigma k}\right)\frac{\partial \epsilon}{\partial x_j}\right] \quad (8)$$

The k–ω turbulence model has a similar structure to the k–ε model and is also widely used in CFD simulations. It employs transport equations for the turbulent kinetic energy kkk and the specific dissipation rate ω\omegaω, given as [12]:

$$\frac{\partial k}{\partial t} + \mu_j \frac{\partial k}{\partial x_j} = P_k - \beta k\omega + \frac{\partial}{\partial x_j}\left[(\nu + \sigma_k \nu_t)\frac{\partial k}{\partial x_j}\right] \quad (9)$$

$$\frac{\partial \omega}{\partial t} + \mu_j \frac{\partial \omega}{\partial x_j} = \alpha\frac{\omega}{k}P_k - \beta\omega^2 + \frac{\partial}{\partial x_j}\left[(\nu + \sigma_k \nu_t)\frac{\partial \omega}{\partial x_j}\right] \quad (10)$$

The k–ω SST (Shear Stress Transport) model, developed by Menter, is specifically designed to accurately capture flows with adverse pressure gradients, in which static pressure increases in the flow direction, leading to flow deceleration, particularly within the boundary layer. This model combines the near-wall accuracy of the k–ω model (inner boundary layer) with the robustness of the k–ε model in the free-stream region through the use of a blending function [8]. In the k–ω SST model, the turbulent viscosity is calculated as:

$$\mu_t = \frac{\rho a^1 k}{\text{Max}\,(a_1\omega, \sqrt{2}S_t F_2)} \quad (11)$$

where $S_t$is the strain-rate magnitude, $a_1 = 0.31$, and $F_2$is the blending function defined as:

$$F_2 = \tanh(\gamma_2^2) \quad (12)$$

where parameter $\gamma_2$is expressed as:

$$\gamma_2 = \text{Max}\left(\frac{2\sqrt{k}}{\beta * \omega d}, \frac{500v}{(d_L)^2\omega}\right) \quad (11)$$

Data Collection

The data utilized in this research consist of propeller geometry data and experimental open-water test data. The propeller geometry parameters include the diameter, number of blades, pitch-to-diameter ratio (P/D), and expanded area ratio (A_E/A_0). These data were obtained from a scaled model of a 60-m high-speed vessel propeller, which was adapted for numerical simulation purposes. The detailed geometric characteristics of the propeller employed in this research are summarized in table 1.

Table 1. Propeller Geometry Data

Parameter	Gawn-Burril Model
Diameter (mm)	116.43
Number of Blades	4
Expanded Area Ratio	0.83
Pitch of Ratio	1.38

In addition, experimental data were obtained from the Indonesian Hydrodynamics Laboratory and were used as reference data for validating the CFD simulation results, particularly for the thrust force (T), torque (Q), and propeller efficiency.

Geometry and Computational Domain Modelling

The geometric modeling process began by importing the propeller geometry data into AutoCAD to generate a two-dimensional (2D) model representing the blade and hub profiles. The 2D propeller model was then transferred to another CAD software package to be converted into a three-dimensional (3D) solid model, which is required for numerical simulation. Subsequently, the solid 3D propeller model was imported into ANSYS SpaceClaim, where the computational domain was defined. The final 3D geometry of the propeller used in this research is shown in fig. 1.

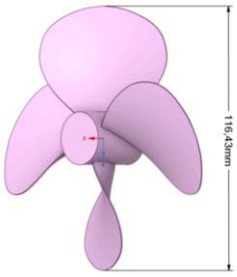

Figure 1. Propeller 3D Model

The computational domain was divided into two regions, namely a rotating domain and a stationary domain. The rotating domain was defined to enclose the propeller and was dimensioned with an upstream length of 0.5D from the propeller plane, a downstream length of 2D, and a domain diameter of 1.5D. These dimensions were selected to ensure proper flow development around the propeller while minimizing numerical interference from domain boundaries. The stationary domain was designed to capture the wake flow generated by the propeller. This domain extended 2D upstream, 8D downstream, and had a diameter of 5D, allowing the propeller slipstream to be fully resolved and preventing artificial boundary effects. The configuration of the computational domain employed in this research is illustrated in fig. 2.

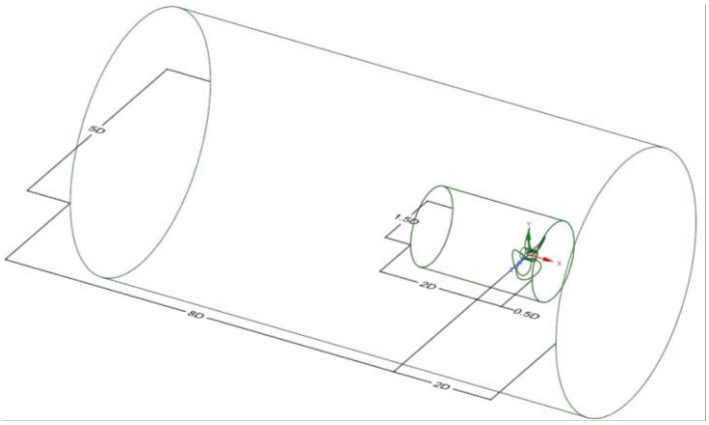

Figure 2. Computational Domain

The dimensions of the computational domain were determined based on previous studies [13], [14] and adapted to the propeller diameter. This configuration was selected to ensure adequate flow development around the propeller and to minimize the influence of boundary effects on the numerical results.

Mesh Generation

The meshing process was performed to discretize the computational domain into finite elements, enabling the numerical solution of the governing fluid-flow equations. A polyhedral mesh was employed in this research, with the addition of inflation layers along the propeller surface to accurately capture boundary-layer phenomena.

Mesh refinement was applied in critical regions, particularly around the blade and hub, to enhance the accuracy of the numerical results. The mesh quality was assessed based on skewness and orthogonal quality parameters in accordance with the recommendations provided by the ANSYS software. The surface mesh and volume mesh distributions of the propeller are illustrated in fig. 3 and fig. 4.

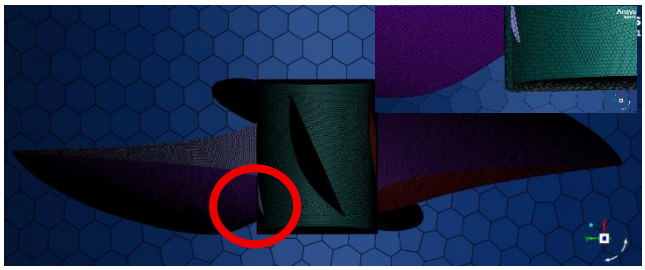

Figure 3. Propeller Surface Mesh

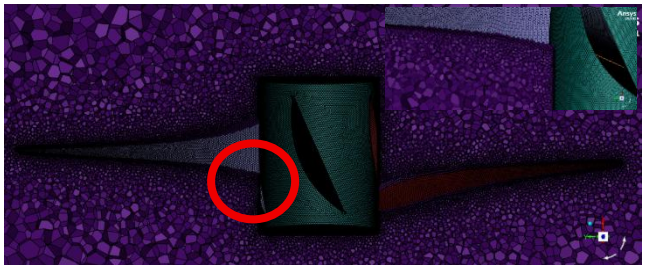

Figure 4. Propeller Volume Mesh

The y^+ values were carefully controlled according to the turbulence model employed. Based on previous studies [15], the k–ε turbulence model was applied using a y^+ range of 30–300, whereas the k–ω and k–ω SST models required y^+ values close to unity ($y^+ \approx 1$) to ensure proper near-wall resolution.

The CFD simulations were performed using ANSYS Fluent under a steady-state assumption. The governing equations solved were the Reynolds-Averaged Navier–Stokes (RANS) equations coupled with three turbulence models, namely k–ε, k–ω, and k–ω SST. The working fluid was seawater, which was assumed to be incompressible with constant density. The applied boundary conditions used in the simulations are summarized in table 2.

Table 2 Boundary Condition

Named Selection	Boundary Condition
Blade	Moving Wall
Hub	Moving Wall
Inlet	Velocity-Inlet
Outlet	Pressure-Outlet
Shroud	Symmetry

The applied boundary conditions were designed to represent the actual operating conditions of an open-water propeller test. A uniform inflow velocity was prescribed at the inlet boundary corresponding to the desired advance coefficient (J). The outlet boundary was defined as a pressure outlet with zero gauge pressure to allow fully developed flow to exit the computational domain. The propeller blade and hub surfaces were modeled as rotating walls with a specified rotational speed, while the outer shroud boundary was defined as a symmetry condition to minimize boundary interference effects. This configuration ensures realistic representation of propeller operation in an unbounded fluid domain.

The discretization scheme employed in the simulations was based on second-order accuracy to enhance numerical precision. Convergence was achieved when the residuals of all governing equations fell below 10^{-5}, and when the computed thrust and torque values exhibited stable behavior with respect to successive iterations. A summary of the numerical and solver settings applied in this research is summarized in table 3.

Table 3 Solver Setup

Named Selection	Solver
Solver type	Pressure Based
Time	Steady
Turbulence model	k-ε, k-ω, k-ω SST
Pressure Velocity Coupling Scheme	Coupled
Gradient	Least Squares Cell Based
Pressure	Second Order
Momentum	Second Order Upwind
Turbulent Kinetic Energy	Second Order Upwind
Specific Dissipation Rate	Second Order Upwind

RESULTS AND DISCUSSION

Verification

Verification was conducted through a Grid Independence Study and Grid Convergence Index analysis to ensure that the simulation results were not influenced by mesh resolution. Several mesh configurations with different numbers of elements were evaluated, and the corresponding results were compared based on the predicted thrust and torque values until only negligible differences were observed.

The Grid Independence Study aims to confirm that the CFD results are independent of the grid density, thereby ensuring that the numerical solutions accurately represent the physical flow behavior. This analysis was performed

for each turbulence model considered in the study, namely k–ε, k–ω, and k–ω SST, with four different mesh resolutions examined for each model. The results of the Grid Independence Study based on K_T for the k–ε, k–ω, and k–ω SST turbulence models are presented in table 4.

Table 4 Grid Independence Study Results

k–ε			k–ω			k–ω SST		
Number of Cell	K_T	Δ	Number of Cell	K_T	Δ	Number of Cell	K_T	Δ
1247744	0.23	-	1286512	0.23	-	1286512	0.23	-
2382065	0.23	0.48%	2425066	0.24	-1.37%	2425066	0.24	-2.04%
4959499	0.23	-0.04%	4932864	0.24	-0.38%	4932864	0.24	-0.53%
10036941	0.23	-0.02%	9876901	0.24	-0.05%	9876901	0.24	-0.07%

The Grid Independence Study for the k–ε turbulence model shows a difference of 0.48% in the K_T between the first and second mesh configurations. The differences in K_T between the second and third meshes, as well as between the third and fourth meshes, decrease progressively, indicating improved solution convergence with increasing grid resolution. The results of the Grid Independence Study based on K_T for the k–ε model are presented graphically in fig. 5.

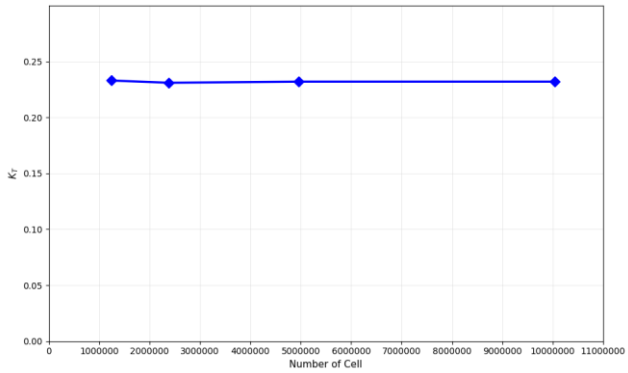

Figure 5. k–ε Grid Independence Study

For the k–ω turbulence model, the Grid Independence Study reveals a difference of –1.37% in the K_T value between the first and second mesh configurations. Similar to the k–ε model, the differences in K_T between second to third and third to fourth meshes become progressively smaller, indicating convergence of the numerical solution. The results of the Grid Independence Study based on K_T for the k–ω model are presented graphically in fig. 6.

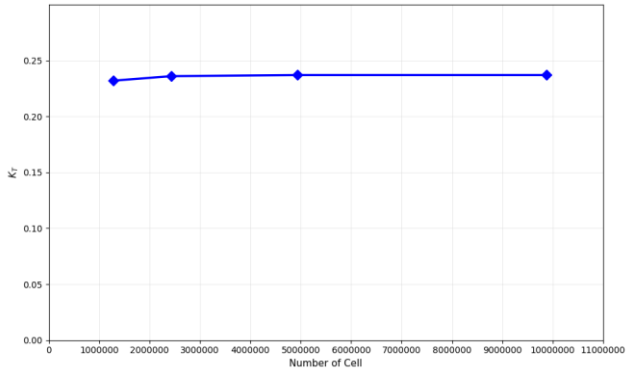

Figure 6. k–ω Grid Independence Study

In the case of the k–ω SST turbulence model, a difference of –2.04% in the K_T value is observed between the first and second mesh configurations. As the mesh resolution is further refined, the differences in K_T between the higher-resolution meshes decrease significantly, confirming mesh-independent behavior. The Grid Independence Study results for the k–ω SST model are presented graphically in fig. 7.

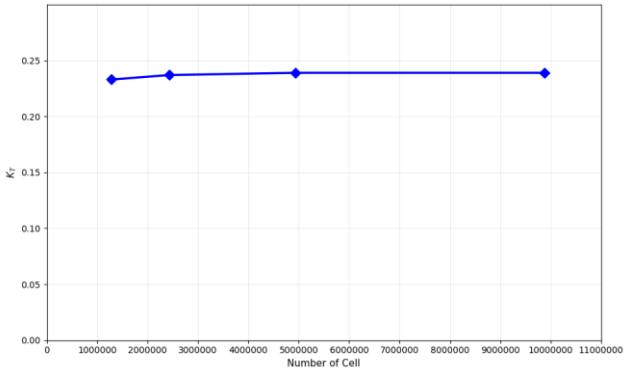

Figure 7. k–ω SST Grid Independence Study

The Grid Convergence Index aims to quantify that the accuracy of the numerical solutions resulting from grid discretization and to provide an estimation of the numerical uncertainty associated with each mesh resolution. The Grid Convergence Index calculation was performed based on the methodology proposed by Roache [16], which is widely used for assessing grid-related numerical uncertainty in CFD studies. The Grid Convergence Index analysis requires three systematically refined mesh levels, which were classified according to mesh quality as coarse, medium, and fine grids. The results of the Grid Convergence Index analysis for the k–ε, k–ω, and k–ω SST turbulence models are summarized in table 5.

Table 5. Grid Convergence Index Results

Quality	k–ε			k–ω			k–ω SST		
	f_{ext} (K_T)	ε (K_T)	GCI (K_T)	f_{ext} (K_T)	ε (K_T)	GCI (K_T)	f_{ext} (K_T)	ε (K_T)	GCI (K_T)
Medium to Fine	0.00010	0.02%	0.03%	0.00013	0.05%	0.01%	0.000194	0.07%	0.01%
Coarse to Medium	0.00019	0.04%	0.05%	0.00103	0.38%	0.07%	0.00145	0.53%	0.10%

Based on the calculation results, the extrapolated relative error for the k–ε turbulence model is 0.04% for the comparison between the coarse and medium meshes and 0.02% for the comparison between the medium and fine meshes. These results indicate that the numerical solution exhibits increasing convergence with mesh refinement. The corresponding Grid Convergence Index (GCI) values for the k–ε model are 0.05% for the coarse-to-medium comparison and 0.03% for the medium-to-fine comparison, both of which are below 1%. This confirms that the numerical errors associated with grid discretization are relatively small and that the solution has reached a grid-independent condition.

For the k–ω turbulence model, the extrapolated relative errors are 0.38% for the coarse-to-medium mesh comparison and 0.05% for the medium-to-fine comparison, indicating improved numerical convergence as the number of mesh elements increases. The corresponding GCI values are 0.07% for the coarse-to-medium comparison and 0.01% for the medium-to-fine comparison. Since both values are well below 1%, it can be concluded that grid discretization errors are minimal and that the numerical solution for the k–ω model is also grid independent.

Similarly, for the k–ω SST turbulence model, extrapolated relative errors of 0.53% and 0.07% are obtained for the coarse-to-medium and medium-to-fine mesh comparisons, respectively. Although the error is slightly higher for the coarser grid, the solution demonstrates good convergence behavior as mesh resolution increases. The calculated GCI values are 0.10% for the coarse-to-medium comparison and 0.01% for the medium-to-fine comparison. The fact that all GCI values remain below 1% indicates that the numerical uncertainty due to grid discretization is negligible and that the simulation results have achieved grid-independent conditions, making them suitable for further analysis.

Based on the Grid Independence Study and Grid Convergence Index, the selected mesh size for the final simulations consisted of approximately 4.9 million cells for the k–ε model, 4.9 million cells for the k–ω model, and 4.9 million cells for the k–ω SST model, which provided a balance between numerical accuracy and computational efficiency.

Simulation Results and Validation

The numerical simulations were performed using a CFD approach based on the RANS equations with three different turbulence models, namely k–ε, k–ω, and k–ω SST. The primary results obtained from the simulations include the K_T, $10K_Q$, and η_0 under specific operating conditions. The simulation results for the k–ε, k–ω, and k–ω SST turbulence models are presented in tables 6, 7, and 8.

Table 6. k–ε Simulation Results

No.	Speed Carriage (m/s)	J	K_T	$10K_Q$	η_o
1	0.414	0.1	0.658	1.329	0.079
2	1.241	0.3	0.586	1.182	0.237
3	2.069	0.5	0.480	0.979	0.390
4	2.896	0.7	0.361	0.779	0.516
5	3.310	0.8	0.297	0.668	0.567
6	3.724	0.9	0.232	0.565	0.587
7	4.138	1	0.185	0.517	0.569
8	4.552	1.1	0.129	0.462	0.489
9	4.965	1.2	0.083	0.407	0.392

Table 7. k–ω Simulation Results

No.	Speed Carriage (m/s)	J	K_T	$10K_Q$	η_o
1	0.414	0.1	0.627	1.270	0.079
2	1.241	0.3	0.586	1.182	0.237
3	2.069	0.5	0.485	0.983	0.393
4	2.896	0.7	0.368	0.780	0.525
5	3.310	0.8	0.304	0.680	0.569
6	3.724	0.9	0.237	0.574	0.591
7	4.138	1	0.189	0.524	0.574
8	4.552	1.1	0.132	0.464	0.497
9	4.965	1.2	0.089	0.408	0.416

Table 8. k–ω SST Simulation Results

No.	Speed Carriage (m/s)	J	K_T	$10K_Q$	η_o
1	0.414	0.1	0.632	1.271	0.079
2	1.241	0.3	0.586	1.182	0.237
3	2.069	0.5	0.489	0.987	0.394
4	2.896	0.7	0.370	0.781	0.528
5	3.310	0.8	0.306	0.685	0.568
6	3.724	0.9	0.239	0.580	0.590
7	4.138	1	0.192	0.530	0.576
8	4.552	1.1	0.135	0.469	0.502
9	4.965	1.2	0.086	0.408	0.405

The validation of the numerical results was performed by comparing the CFD simulation outputs with experimental open-water test data. The comparison was carried out using the Root Mean Square Error (RMSE) method as a quantitative metric to evaluate the deviation between the experimental and numerical results, following the approach proposed by Indiaryanto et al. [17]. The primary parameters considered in the validation process were the K_T, $10K_Q$ and η_o, which collectively represent the effectiveness of the propeller in converting engine power into useful thrust. The RMSE formulation employed in this study is given as follows [17]:

$$\mathrm{RMSE} = \sqrt{\frac{1}{N}\sum_{i=1}^{N}(X_{i,sim} - X_{i,exp})^2} \tag{12}$$

where N denotes the number of J values considered, $X_{i,sim}$ represents the simulation result, and $X_{i,exp}$ denotes the corresponding experimental value. The analysis was performed for the simulation results obtained using the three turbulence models employed in this study, namely the k–ε, k–ω, and k–ω SST models. The validation results of the CFD simulations against the experimental data for the k–ε, k–ω, and k–ω SST turbulence models are presented in tables 9, 10, and 11.

Table 9. k–ε Validation

No.	Speed Carriage (m/s)	J	K_T	$10K_Q$	η_0
1	0.414	0.1	0.00001	0.00011	0.00000
2	1.241	0.3	0.00016	0.00073	0.00000
3	2.069	0.5	0.00005	0.00011	0.00000
4	2.896	0.7	0.00001	0.00001	0.00000
5	3.310	0.8	0.00004	0.00014	0.00001
6	3.724	0.9	0.00026	0.00047	0.00030
7	4.138	1	0.00029	0.00044	0.00080
8	4.552	1.1	0.00026	0.00028	0.00175
9	4.965	1.2	0.00014	0.00001	0.00269
	RMSE		1.16%	1.60%	2.49%

Table 10. k–ω Validation

No.	Speed Carriage (m/s)	J	K_T	$10K_Q$	η_0
1	0.414	0.1	0.00079	0.00232	0.00000
2	1.241	0.3	0.00016	0.00072	0.00000
3	2.069	0.5	0.00014	0.00022	0.00001
4	2.896	0.7	0.00002	0.00001	0.00006
5	3.310	0.8	0.00000	0.00000	0.00000
6	3.724	0.9	0.00012	0.00015	0.00020
7	4.138	1	0.00017	0.00021	0.00053
8	4.552	1.1	0.00018	0.00020	0.00116
9	4.965	1.2	0.00004	0.00000	0.00075
	RMSE		1.34%	2.06%	1.74%

Table 11. k–ω SST Validation

No.	Speed Carriage (m/s)	J	K_T	$10K_Q$	η_0
1	0.414	0.1	0.00543	0.00222	0.00000
2	1.241	0.3	0.00016	0.00072	0.00000
3	2.069	0.5	0.00026	0.00037	0.00003
4	2.896	0.7	0.00004	0.00000	0.00010
5	3.310	0.8	0.00000	0.00003	0.00000
6	3.724	0.9	0.00008	0.00004	0.00023
7	4.138	1	0.00010	0.00006	0.00048
8	4.552	1.1	0.00011	0.00009	0.00079
9	4.965	1.2	0.00008	0.00000	0.00153
	RMSE		1.24%	1.98%	1.88%

Based on the RMSE calculations, the k–ε turbulence model yields RMSE values of 1.16% for the K_T, 1.60% for the $10K_Q$, and 2.49% for η_0. For the k–ω turbulence model, the RMSE values obtained are 1.34% for K_T, 2.06% for $10K_Q$, and 1.74% for η_0. Meanwhile, the k–ω SST turbulence model results in RMSE values of 1.24% for K_T, 1.98% for $10K_Q$, and 1.88% for η_0. For clearer comparison and visualization of the validation results, the RMSE distributions for the k–ε, k–ω, and k–ω SST models are illustrated in figs. 8, 9, and 10.

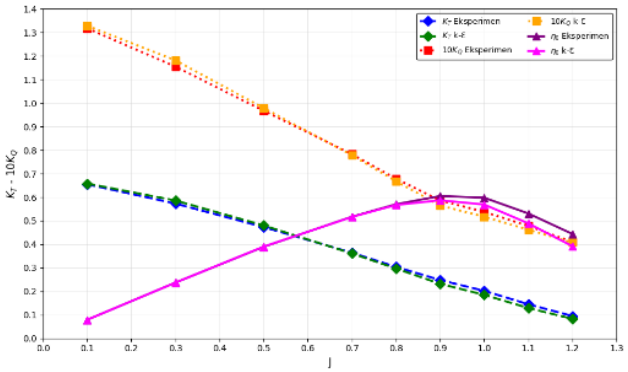

Figure 8. Comparison of k–ε Simulation Results

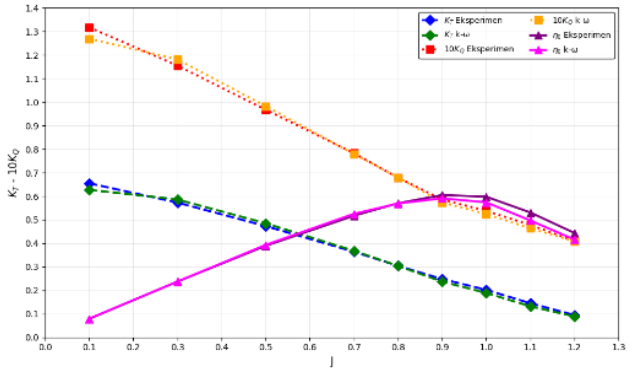

Figure 9. Comparison of k–ω Simulation Results

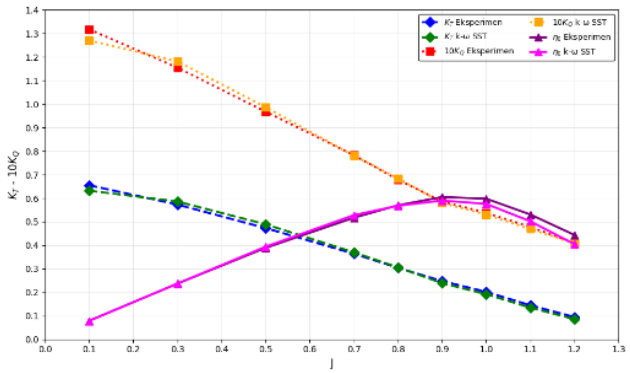

Figure 10. Comparison of k–ω SST Simulation Results

Efficiency (η_0) represents the performance of the propeller in converting input power into useful thrust. Based on table 6, 7, and 8, the efficiency values range from 0.079 to approximately 0.591, showing a clear trend of increasing efficiency with increasing advance ratio (J) up to an optimum point, followed by a gradual decline. At low J values, the efficiency is very small due to suboptimal flow conditions, while at intermediate J values, the propeller operates more effectively, reaching peak efficiency. Beyond the optimal region, efficiency decreases as flow conditions become less favorable, indicating reduced propulsive performance. Furthermore, the efficiency results for each turbulence model can be clearly observed in table 12, which summarizes the comparison across all tested conditions.

Table 12 Efficiency Results of each Turbulence Model

No.	Speed Carriage (m/s)	J	η_0 k–ε	η_0 k–ω	η_0 k–ω SST
1	0.414	0.1	0.079	0.079	0.079
2	1.241	0.3	0.237	0.237	0.237
3	2.069	0.5	0.390	0.393	0.394
4	2.896	0.7	0.516	0.525	0.528
5	3.310	0.8	0.567	0.569	0.568
6	3.724	0.9	0.587	0.591	0.590
7	4.138	1	0.569	0.574	0.576
8	4.552	1.1	0.489	0.497	0.502
9	4.965	1.2	0.392	0.416	0.405

Based on tabel 12, the efficiency (η_0) of the three turbulence models, k–ε, k–ω, and k–ω SST shows a generally similar trend with respect to the increase in the advance ratio (J). At low J values (0.1–0.3), all three models produce nearly identical efficiency values, ranging from about 0.079 to 0.237, indicating that at low-speed conditions, differences in turbulence modeling have minimal impact on the predicted efficiency.

As J increases to approximately 0.7–1.0, the efficiency of all models rises significantly. In this range, the k–ω and k–ω SST models tend to produce slightly higher efficiency values compared to the k–ε model. For example, at J = 0.9, the efficiency predicted by k–ε is 0.587, while k–ω and k–ω SST give 0.591 and 0.590, respectively. This suggests that k–ω-based models are more sensitive in capturing near-wall flow phenomena, resulting in slightly improved efficiency predictions.

Beyond the peak region at around J = 0.9–1.0, the efficiency of all models decreases consistently up to J = 1.2. In this region, differences among the models become more noticeable. The k–ω SST model generally provides

intermediate results between k–ε and k–ω, indicating a more balanced and stable prediction. Overall, the graph demonstrates that while all three models follow the same trend, k–ω and k–ω SST yield slightly higher and smoother efficiency predictions, particularly near optimal operating conditions. For further clarification, it can be seen in fig. 11.

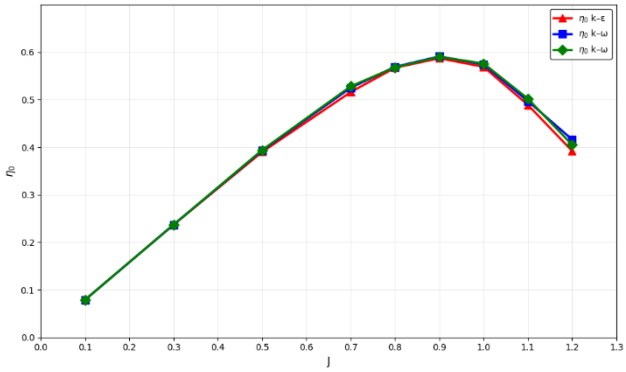

Figure 11. Comparison of each Turbulence Model

Flow-Field Characteristics

The flow characteristics around the propeller were analyzed using velocity and pressure contours. The visualization results reveal flow acceleration on the blade suction side and an increase in pressure on the pressure side, which represent the fundamental mechanism of thrust generation in marine propellers. Fig. 12 presents the static pressure distribution on the pressure side of the blade predicted by the k–ε turbulence model, while the corresponding suction-side pressure distribution is shown in fig. 13. The k–ε model predicts a relatively smooth pressure distribution over the blade surface.

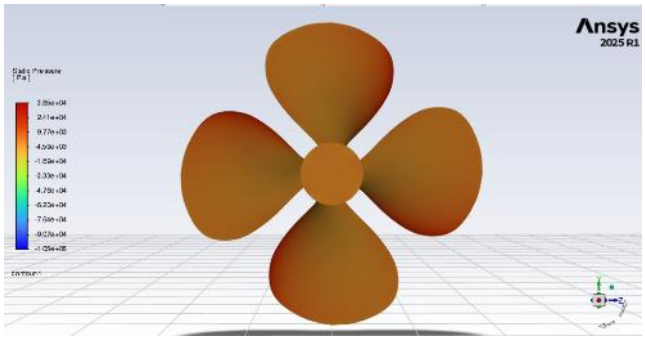

Figure 12 Static Pressure Distribution on the Pressure Side of k–ε

As a result, neither the suction peak on the suction side nor the pressure peak on the pressure side appears as a sharp gradient. This smoothing characteristic is consistent with the findings reported in [18], where it was shown that although the k–ε turbulence model can reasonably predict the overall pressure distribution on the blade surface, it tends to attenuate pressure gradients in critical regions. As a consequence, the predicted high- and low-pressure peaks become less pronounced. This limitation affects torque prediction, since torque is highly sensitive to the pressure distribution and shear forces, particularly in the blade tip region.

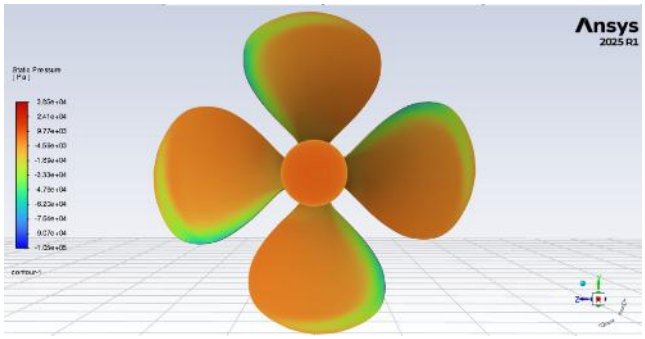

Figure 13 Static Pressure Distribution on the Suction Side of k–ε

The pressure distribution predicted by the k–ω turbulence model is shown in fig. 14 (pressure side) and fig. 15 (suction side). Compared to the k–ε model, the k–ω model is capable of capturing blade loading with sharper pressure gradients, especially in the outer blade regions that contribute significantly to torque generation. On the suction side, a distinct low-pressure region is observed near the leading edge, indicated by green-to-blue contours in fig. 14. The transition between the low-pressure suction region and the surrounding higher-pressure areas is notably steeper, indicating stronger pressure gradients along the blade chord. This behavior is consistent with the observations reported in [19], where it was demonstrated that the k–ω turbulence model provides improved near-wall resolution and enhanced capability in predicting pressure variations near the leading edge and suction side of the blade.

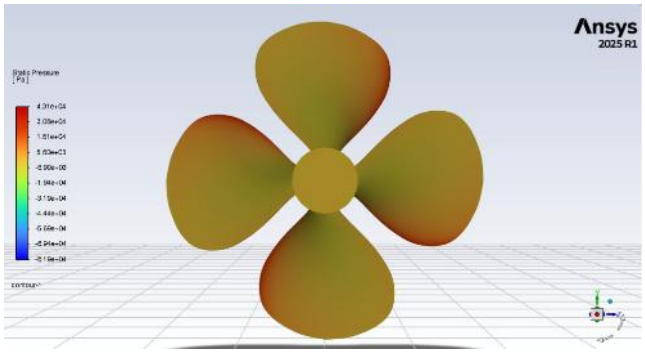

Figure 14 Static Pressure Distribution on the Pressure Side of k–ω

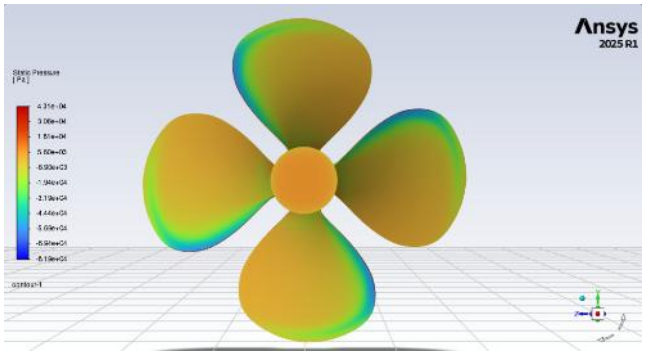

Figure 15 Static Pressure Distribution on the Suction Side of k–ω

The static pressure distributions predicted by the k–ω SST turbulence model are illustrated in fig. 16 (pressure side) and fig. 17 (suction side). Among the three turbulence models examined, the k–ω SST model provides the most accurate representation of blade loading across the entire blade surface. On the suction side (fig. 16), the low-pressure region is more pronounced and sharply defined, particularly from the leading edge to the mid-chord region, as indicated by distinct green-to-blue color gradients. This region represents a strong suction effect generated by the blade camber. Moreover, the transition between the low-pressure zone and the surrounding higher-pressure region (yellow to orange) is noticeably steeper than that predicted by the k–ε and k–ω models, indicating a more accurate prediction of pressure and velocity gradients.

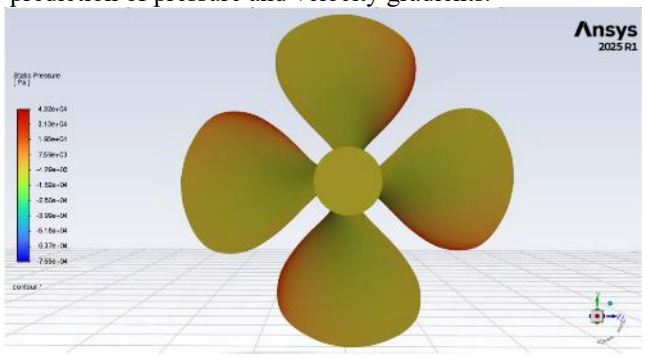

Figure 16 Static Pressure Distribution on the Pressure Side of k–ω SST

As reported in [20], the k–ω SST turbulence model is particularly well suited for simulating marine propellers operating under rotating flow conditions and adverse pressure gradients, as it combines the near-wall accuracy of

the k–ω model with the robustness of the k–ε model in the free-stream region. The pressure-distribution results obtained in this study further confirm the superior capability of the k–ω SST model in capturing complex flow phenomena associated with marine propellers.

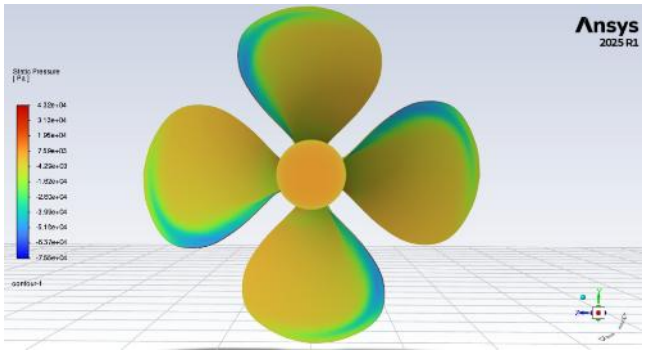

Figure 17 Static Pressure Distribution on the Suction Side of k–ω SST

In addition to the pressure distribution, the formation of strong vortex structures at the blade tip (tip vortex) was clearly identified. These vortical structures contribute significantly to energy losses within the system, as they increase rotational resistance acting on the propeller, thereby affecting the generated torque.

For the k–ε turbulence model, the vortex structures are predicted with a relatively diffuse and smooth character. The vortex core is not sharply defined, and the spiral pathlines do not exhibit a highly concentrated center. This behavior is inherent to the characteristics of the k–ε model, which tends to smooth velocity and pressure gradients due to its reliance on wall-function approaches. As reported in [21], the velocity distribution around the vortex core predicted by the k–ε model is highly sensitive to turbulence-modeling choices, with tangential velocity gradients appearing smoother and less pronounced. Consequently, the rotational intensity within the vortex core is under-predicted compared to the actual physical flow.

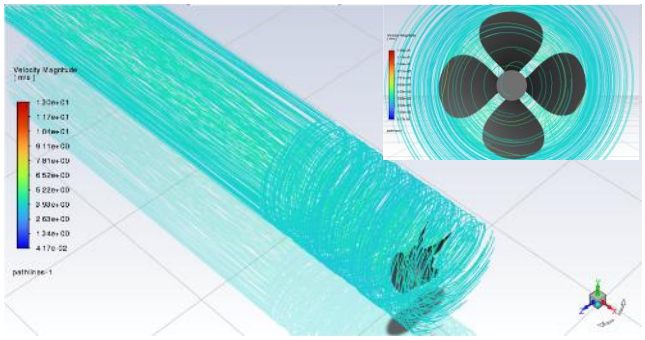

Figure 18 Flow pattern predicted by the k–ε

In contrast, the k–ω turbulence model exhibits sharper and more concentrated vortex structures, particularly in the representation of the tip vortex and hub vortex cores. The resulting spiral pathlines are more clearly defined and tightly wound, with a steeper transition between the vortex core and the surrounding flow. This indicates that the k–ω model, benefiting from its low-Reynolds-number formulation and improved near-wall resolution, is better able to resolve rotational flow near the blade tip compared to the k–ε model, which relies on wall-function approaches. As reported in [21], the k–ω model provides a more accurate and concentrated representation of tip vortices. Furthermore, the tangential velocity distribution around the vortex core predicted by the k–ω model is sharper and exhibits higher peak values, indicating stronger rotational intensity concentrated within a narrower core region, which more closely reflects the physical behavior of propeller-induced vortices.

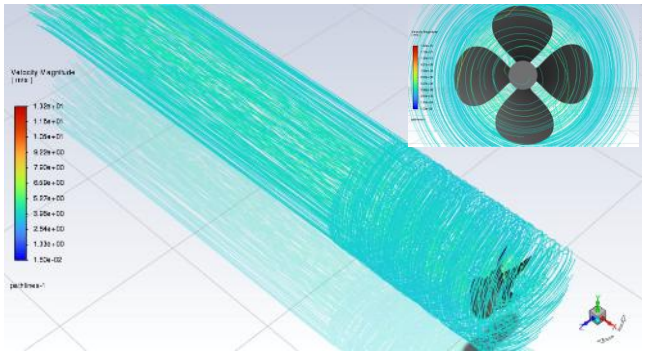

Figure 19 Flow pattern predicted by the k–ω

Among the three turbulence models examined, the k–ω SST turbulence model demonstrates the sharpest, most concentrated, and most well-structured vortex representation, particularly for both the tip vortex and the hub vortex. The spiral pathlines appear dense and well defined, with vortex cores that are clearly identifiable and highly concentrated. The transition between the vortex core and the surrounding flow is also noticeably steeper, indicating that velocity gradients and pressure variations are predicted with the highest level of precision. This superior performance can be attributed to the hybrid formulation of the k–ω SST model, which combines the near-wall accuracy of the k–ω model with the numerical stability of the k–ε model in the free-stream region, thereby enabling an optimal flow representation throughout the computational domain. As reported in [21], eddy-viscosity-based turbulence models such as k–ω SST are capable of accurately capturing tip-vortex structures for engineering applications, provided that sufficient grid resolution is employed. The results obtained in this study further confirm that, when combined with an appropriately refined mesh, the k–ω SST model achieves superior accuracy and structural detail in predicting propeller wake vortex characteristics.

CONCLUSION

This research demonstrates that the selection of turbulence models significantly influences the accuracy of CFD-based marine propeller performance prediction. Among the three RANS models investigated, the k–ω SST model shows the most reliable performance across the entire operating range, particularly in capturing pressure distribution and wake vortex structures. The findings contribute to improving CFD best practices for marine propeller analysis and support the application of the k–ω SST model in engineering design and evaluation of Gawn Series propellers. Future research is recommended to extend the analysis to transient simulations, cavitation prediction, and propeller–hull interaction to further enhance predictive capability.

ACKNOWLEDGEMENT

The authors sincerely thank the National Research and Innovation Agency for provided the experimental data.

REFERENCES

[1] D. R. Aldara, T. Irmiyana, A. L. F. Faisal, A. Ghofur, and R. Insani, “Strategi optimalisasi pemilihan propeller B-series untuk kapal: Studi kasus kapal tangker [B-series propeller selection optimization strategy for ships: A case study of a tanker]” Jurnal Teknik, vol. 13, no. 2, pp. 234–242, 2023.

[2] F. Tillig, J. W. Ringsberg, W. Mao, and B. Ramne, “A generic energy systems model for efficient ship design and operation,” *Proceedings of the Institution of Mechanical Engineers, Part M: Journal of Engineering for the Maritime Environment*, vol. 231, no. 2, pp. 649–666, 2017, doi: 10.1177/1475090216680672.

[3] R. Geertsma, R. R. Negenborn, K. Visser, and M. Loonstijn, “Pitch control for ships with diesel mechanical and hybrid propulsion: Modelling, validation and performance quantification,” *Applied Energy*, vol. 206, pp. 1609–1631, Nov. 2017, doi: 10.1016/j.apenergy.2017.09.103.

[4] I. Abdilla, C. Abar, D. Chrismianto, and P. Manik, “Analisa perbandingan propeller kapal selam tipe B-series dan AU-outline Gawn series pada kapal selam midget type 150M untuk mengoptimalkan kinerja kapal selam dengan metode CFD,” Jurnal Teknik Perkapalan, vol. 3, no. 4, 2015.

[5] M. Rakhim, A. Baidowi, and M. Indiaryanto, "Effect of Gawn Series Propeller Camber Ratio Variations on Fuel Consumption Using Engine Propeller Matching," *International Journal of Marine Engineering Innovation and Research*, vol. 11, no. 1, pp. 37–56, Mar. 2026, doi: 10.12962/j25481479.v11i1.

[6] N. Nurhadi, H. Zen, and S. Sumarsono, "Study of engine propeller matching for high-speed vessel with Gawn series propeller," EPI International Journal of Engineering, vol. 1, no. 1, pp. 39–42, 2018, doi: 10.25042/epi-ije.022018.07

[7] C. Kusuma, I. M. Ariana, W. H. Nugroho, E. B. Djatmiko, A. A. Masroeri, and Sutardi, "Design Propeller Of Fast Missile Boat 60 M By Using Gawn Series," *IOP Conference Series: Materials Science and Engineering*, vol. 1052, no. 1, p. 012026, 2021, doi: 10.1088/1757-899X/1052/1/012026.

[8] K. Suastika, Dinamika Fluida Komputasi Metode Volume Hingga. Surabaya, Indonesia: ITS Press, 2023.

[9] M. M. Helal, T. M. Ahmed, A. A. Banawan, and M. A. Kotb, "Numerical prediction of the performance of marine propellers using computational fluid dynamics simulation with transition-sensitive turbulence model," Proc. IMechE, Part M: Journal of Engineering for the Maritime Environment, vol. 233, no. 2, pp. 515–527, 2019, doi:10.1177/1475090218763199

[10] N. Shalom, "CFD analysis on marine propeller with various geometrical conditions," Recent Research Reviews Journal, vol. 2, no. 2, pp. 242–255, 2023, doi:10.36548/rrrj.2023.2.002

[11] J. S. Carlton, Marine Propellers and Propulsion, 2nd ed. Oxford, U.K.: Butterworth-Heinemann, 2007, pp. 1–533.

[12] S. B. Pope, Turbulent Flows. Cambridge, U.K.: Cambridge University Press, 2001, p. 773.

[13] H. Mikkelsen, M. L. Steffensen, "Full scale validation of CFD model of self-propelled ship," M.S. thesis, Technical University of Denmark, Lyngby, Denmark, Jun. 2016, doi:10.13140/RG.2.2.25689.21607

[14] A. M. Ghoniem, A. S. A. Elazm, M. I. Benaya, and S. A. Mohamed, "Effect of salinity on marine propeller performance," Journal of Physics: Conference Series, vol. 2616, no. 1, pp. 1–8, 2023, doi:10.1088/1742-6596/2616/1/012016

[15] Y. Li, S. Yang, F. Feng, and K. Tagawa, "A review on numerical simulation based on CFD technology of aerodynamic characteristics of straight-bladed vertical axis wind turbines," Energy Reports, vol. 9, pp. 4360–4379, 2023, doi: 10.25042/epi-ije.052018.07

[16] P. J. Roache, "Perspective: A method for uniform reporting of grid refinement studies," Journal of Fluids Engineering, vol. 116, pp. 405–413, 1994, doi: 10.1115/1.2910291.

[17] M. Indiariyanto, K. Suastika, T. A. Setyanto, and P. H. N. Prayoga, "Comparison of the hydrodynamic performance of three different propeller foil types: NACA 66 (Mod), ogival and NACA symmetrical section," CFD Letters, vol. 17, no. 10, pp. 168–183, 2025, doi: 10.37934/cfdl.17.10.168183

[18] X. Wang and K. Walters, "Computational analysis of marine-propeller performance using transition-sensitive turbulence modeling," Journal of Fluids Engineering, vol. 134, no. 7, pp. 1–10, 2012, doi: 10.1115/1.4005729.

[19] C. Parra, "Numerical investigation of the hydrodynamic performances of marine propeller," M.S. thesis, 2013, pp. 1–104.

[20] R. Mehdipour, "Simulating propeller and propeller–hull interaction in OpenFOAM," M.S. thesis, Royal Institute of Technology (KTH), Stockholm, Sweden, 2013, pp. 1–45.

[21] H. Peng, W. Qiu, and S. Ni, "Effect of turbulence models on RANS computation of propeller vortex flow," Ocean Engineering, vol. 72, pp. 304–317, 2013, doi: 10.1016/j.oceaneng.2013.04.008.